EOARD Grant 063008

Final Report

Modeling of THz quantum cascade lasers for room temperature operation

Principal investigator:

Prof. Dr. Paolo Lugli

Institute for Nanoelectronics

Technical University Munich

Arcisstrasse 21, D-80333 München, Germany

January 10th, 2007

REPORT DOCUMENTATION PAGE

Form Approved OMB No. 0704-0188

Public reporting burden for this collection of information is estimated to average 1 hour per response, including the time for reviewing instructions, searching existing data sources, gathering and maintaining the data needed, and completing and reviewing the collection of information. Send comments regarding this burden estimate or any other aspect of this collection of information, including suggestions for reducing the burden, to Department of Defense, Washington Headquarters Services, Directorate for Information Operations and Reports (0704-0188), 1215 Jefferson Davis Highway, Suite 1204, Arlington, VA 22202-4302. Respondents should be aware that notwithstanding any other provision of law, no person shall be subject to any penalty for failing to comply with a collection of information if it does not display a currently valid OMB control number.
PLEASE DO NOT RETURN YOUR FORM TO THE ABOVE ADDRESS.

1. REPORT DATE *(DD-MM-YYYY)* 20-02-2007	2. REPORT TYPE Final Report	3. DATES COVERED *(From – To)* 1 January 2006 - 01-Jan-07

4. TITLE AND SUBTITLE Modeling of THz quantum cascade lasers for room temperature operation	5a. CONTRACT NUMBER FA8655-06-1-3008
	5b. GRANT NUMBER
	5c. PROGRAM ELEMENT NUMBER
6. AUTHOR(S) Professor Paolo - Lugli	5d. PROJECT NUMBER
	5d. TASK NUMBER
	5e. WORK UNIT NUMBER

7. PERFORMING ORGANIZATION NAME(S) AND ADDRESS(ES) Institute for Nanoelectronics Archistrasse 21 Munich 80333 Germany	8. PERFORMING ORGANIZATION REPORT NUMBER N/A

9. SPONSORING/MONITORING AGENCY NAME(S) AND ADDRESS(ES) EOARD PSC 821 BOX 14 FPO AE 09421-0014	10. SPONSOR/MONITOR'S ACRONYM(S)
	11. SPONSOR/MONITOR'S REPORT NUMBER(S) Grant 06-3008

12. DISTRIBUTION/AVAILABILITY STATEMENT

Approved for public release; distribution is unlimited.

13. SUPPLEMENTARY NOTES

14. ABSTRACT: The simulation comprises two main tasks, the evaluation of the carrier wave functions, and the simulation of the carrier and radiation transport in the structure. These tasks are implemented in two different modules, which have to be especially adapted to the silicon-germanium material system or newly developed. In the first module, the energy levels and carrier wave functions are determined. These are needed for the evaluation of the scattering processes in the carrier transport simulation and the transition probabilities associated with the radiation transport. QCLs consist of a periodically repeated multiple quantum well structure, resulting in quantization effects due to the carrier confinement in the wells. In a first version of the tool, an effective mass description of the semiconductor materials is used, and the carrier eigenstates are found with a Schrödinger-Poisson solver. Such a solver has already been developed at our institute. One important goal is a further improvement of the algorithm to provide a better numerical stability, and an extension as to take into account both the heavy hole and the light hole band for the simulation of Si/SiGe QCLs. In the second module, the carrier transport is evaluated. The motion of the carriers in the structure is subject to the applied electric and magnetic fields and various scattering mechanisms. For the simulation of the particle transport in the structure, the Monte Carlo technique is used. Characteristic for this method is the stochastic evaluation of the scattering events. A Monte Carlo solver, based on the effective mass approximation, has already been developed at our institute [3]. For the simulation of Si/SiGe lasers, it has to be extended as to take into account both the heavy hole and the light hole band, as well as scattering mechanisms which are specific to the silicon-germanium system. A reliable prediction of the gain and the carrier distribution requires the coupled simulation of the carrier transport in the structure and the radiation transport in the laser cavity. The gain depends on the carrier distribution, which again is affected by the absorption and emission processes. Thus, a further important step is the implementation of the effects due to photon absorption and emission, which are not yet considered in the current version of the solver.

15. SUBJECT TERMS
EOARD, Quantum Cascade Laser, semiconductor lasers, sub-millimeter waves, terahertz technology

16. SECURITY CLASSIFICATION OF:			17. LIMITATION OF ABSTRACT	18, NUMBER OF PAGES	19a. NAME OF RESPONSIBLE PERSON DONALD J SMITH
a. REPORT UNCLAS	b. ABSTRACT UNCLAS	c. THIS PAGE UNCLAS	UL	18	19b. TELEPHONE NUMBER *(Include area code)* +44 (0)20 7514 4953

Standard Form 298 (Rev. 8/98)
Prescribed by ANSI Std. Z39-18

Introduction

The terahertz frequency region spans the range between 0.3 and 10 THz. There is a considerable need for practical THz sources, notably for defence-oriented applications such as the detection of biological and chemical materials, imaging through persons or container walls, and secure short-distance communication through the atmosphere. However, electronics-based radiation sources generally operate at frequencies below the THz regime, while photonic sources usually are efficient above – thus, the THz region is also referred to as "terahertz gap" between electronics and photonics. The ideal THz source is compact and inexpensive, operates at room temperature, and emits at least a few mW of coherent radiation. Quantum cascade lasers (QCLs) are based on artificial intersubband transitions which can be custom tailored for the specific application, and thus have an enormous potential as compact and efficient THz sources. For a more detailed overview about THz technology and quantum cascade lasers, see the Introduction and Sections 1 – 2 of the first interim report.

A few years ago, the first QCL operating at terahertz wavelengths was demonstrated, working up to a temperature of 45 K with a maximum output power of 2 mW at 4.4 THz [1]. Much progress has been made since, but the low operating temperatures associated with THz QCLs have remained a major challenge. This is due to the longitudinal-optical (LO) phonon scattering, which dominates carrier transport at medium and high temperatures and increases exponentially with temperature. The most promising approach to overcome this issue is a new scheme based on LO phonon scattering depopulation, and various structures have been successfully demonstrated [2-5]. This design takes advantage of the strong LO phonon scattering, exploiting the mechanism for an efficient depletion of the lower laser level. Here, the collector state directly below the lower laser level is separated from the next lower level by at least the LO phonon energy, enabling efficient depletion of the lower radiative state by LO phonon scattering and reducing thermal backfilling. This overcomes the limitations associated with the conventional bound-to-continuum and chirped superlattice designs, where thermal backfilling of the lower radiative state prevents high temperature performance. A record operating temperature of 164 K in pulsed and 117 K in continuous wave (cw) operation has been reached with a GaAs-based structure [5].

A different approach are QCLs based on the Si/SiGe material system [6]. The hope is that potentially higher operation temperatures can be reached due to the absence of polar phonon scattering in the material, resulting in a weaker temperature dependence of carrier transport processes. However, a working Si/SiGe QCL has not yet been demonstrated; only electroluminescence could be achieved in various Si/SiGe structures. [7,8].

In the following, we will thoroughly investigate existing experimental GaAs-based resonant-LO phonon depopulation structures and compare the

simulation results to experiments. Furthermore, the detrimental effects for high temperature operation will be explored. Finally, some Si/SiGe structures will be theoretically investigated.

1. Investigation of GaAs-based resonant-phonon depopulation THz QCLs

1.1 The Monte Carlo program

For the analysis, an in-house ensemble Monte Carlo (MC) simulation program is used [9,10], which has been developed further within the framework of this project. The subband energies and wavefunctions of the structure are calculated with a Schrödinger-Poisson solver, coupled to the MC simulation. The essential scattering mechanisms due to electron-electron, electron-LO phonon, and electron-acoustic phonon interactions are considered as described in Ref 10. Intercarrier scattering is implemented based on the Born approximation [11,12], also taking into account screening effects [13]. Non-equilibrium phonon distributions are explicitly considered, and the Pauli's exclusion principle is also accounted for. Due to the relatively low electron densities, the influence of such mechanisms is negligible. Periodic boundary conditions are used, i.e., electrons coming out from one side of the device are automatically injected into the equivalent level on the opposite side [14]. For a more detailed description of the code, see Sections 3.1 and 3.2 of the first interim report.

1.2 The resonant-phonon depopulation scheme

Fig. 1(a) shows one period of the conduction band structure of a 2.8 THz resonant-phonon depopulation QCL [4] calculated at 11.7 kV/cm; the band profiles of the other GaAs-based structures discussed in this report are similar. The upper and lower levels of the lasing transition around 2.8 THz are labeled 5 and 4, respectively. Efficient depopulation of level 4 is achieved via the collector state 3, which is in turn separated from the levels 2 and 1 by roughly the optical phonon energy (36 meV), thus enabling efficient depletion to these levels by optical phonon scattering. Parasitic channels counteracting the onset of population inversion between levels 5 and 4 are provided by the injection from levels 1' and 2' (i.e., the replica of levels 1 and 2 situated in the adjacent period on the right side of Fig. 1(a)) into levels 1 – 4, and by scattering processes from the upper laser level to the states below. In Fig. 1(b), the level energies of the 2.8 THz design are shown as a function of the applied electric field. The strong anticrossings between level 5 and the injection levels 2' and 1' around 9.9 and 11 kV/cm facilitate a selective injection into the upper laser level, leading to a reduction of the parasitic channels. Around 7.6 kV/cm, there is an additional anticrossing between levels 1' and 4, causing a strong parasitic injection into the lower laser level [15]. The energy difference between the collector state 3 and the injector state 2 (1) increases from 28 meV (36 meV) for 7 kV/cm to 40 meV (44 meV) for 13

kV/cm, enabling an efficient LO-phonon-induced depletion of the lower laser level especially for biases > 10 kV/cm.
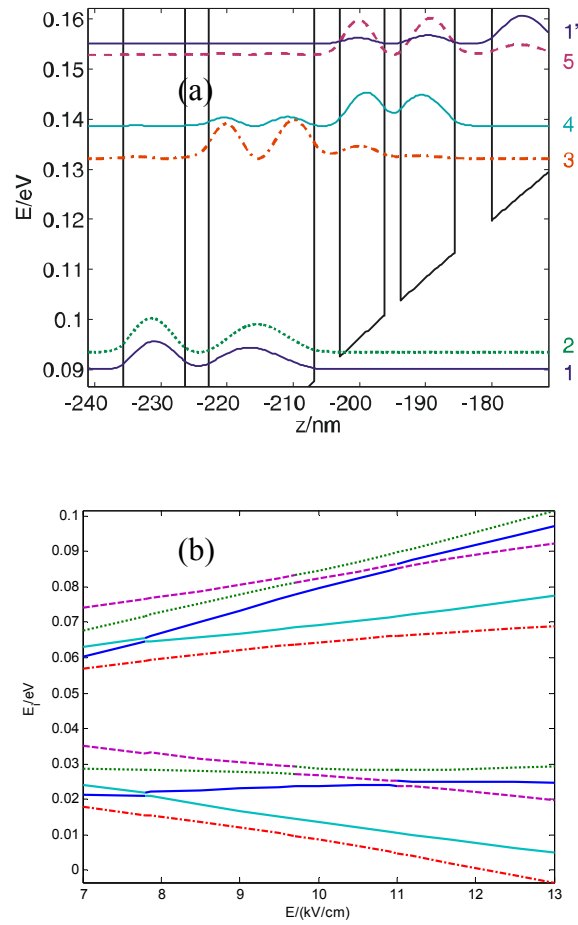

Fig. 1. (a) Conduction band profile and probability densities of a 2.8 THz QCL based on a phonon depopulation scheme at 11.7 kV/cm. The layer thicknesses of one period, starting from the injection barrier, are 56/93/36/160/39/67/25/81 [Å]. The underlined layer is doped at $n=1.9 \times 10^{16}$ cm^{-3} and the sheet density for one period is $n_{2D}=3 \times 10^{10}$ cm^{-2}. (b) Level energies as a function of the applied field for two periods of the 2.8 THz structure.

1.3 Investigation of optimized experimental QCL structures

In the following, we theoretically investigate already existing experimental resonant-phonon depopulation structures. This enables us to identify the important effects dominating carrier transport in such structures and to compare our simulation results to experimental data. We choose three GaAs/Al$_{0.15}$Ga$_{0.85}$As THz QCL structures based on the above scheme and fabricated with high-confinement low-loss double metal waveguides. An experimental comparison between these structures was already carried out [4] and motivates our theoretical comparative investigation.

Figure 2 shows MC simulation results for the 2.8 THz structure at a lattice temperature of 100 K. The sampling electric fields were chosen as to avoid

the excessive current spikes emerging near narrow anticrossings in MC simulations [15]. It should be pointed out that sharp anticrossing features are an artifact of the Schrödinger solution in the absence of broadening mechanisms (such as those provided by surface roughness). If a more precise quantum mechanical approach were used [16], much smoother features would be observed, that would nevertheless not drastically modify our analysis. In Fig. 2(a), the difference and ratio of the relative population in the upper (p_5) and lower (p_4) laser levels is displayed, with $\Delta p_{54}=p_5-p_4$. The current density in Fig. 2(b) exhibits a parasitic peak (not shown) around the 1' - 4 anticrossing and a local minimum at 8.25 kV/cm. It reaches its maximum around the two anticrossings of level 5 with the injector states 1' and 2', where the injection into subband 5 is most efficient. In addition, the energy difference between the collector state 3 and levels 2,1 is designed to reach the LO phonon energy in this bias range and thus become favorable for LO phonon-induced depletion of level 4. These two effects combine to yield a large population difference Δp_{54} and thus a high material gain between 10 and 11 kV/cm.
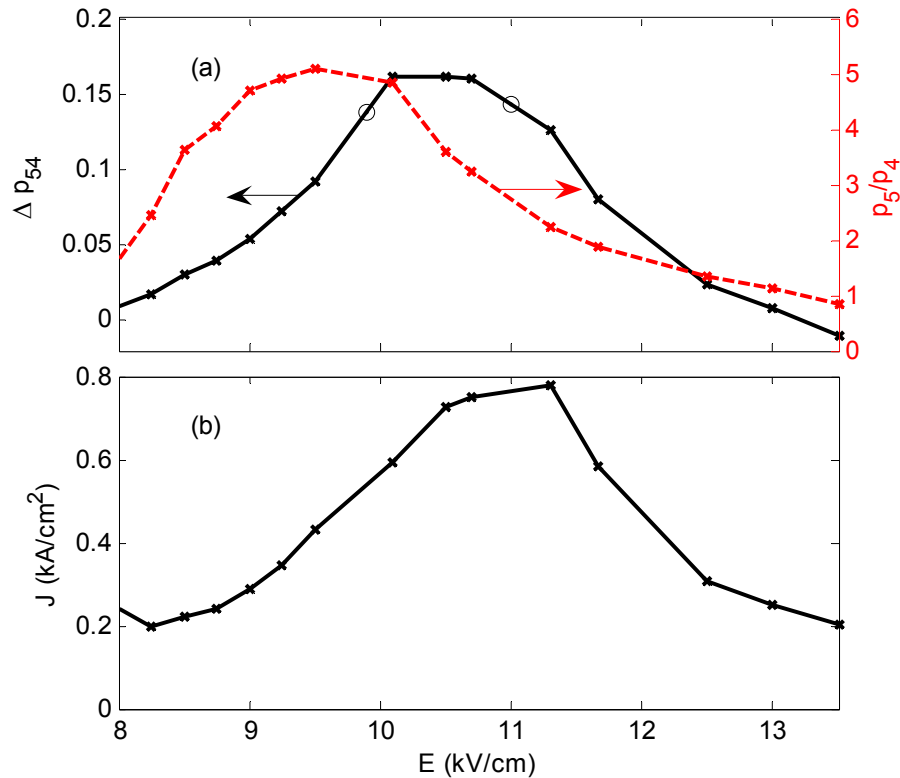

Fig. 2. Simulation results for the 2.8 THz structure as a function of the applied field (E). The crosses mark the sampling points; the lines are guide to the eye. (a) Relative population difference (solid line) and inversion (dashed line) between the upper and lower laser level. The circles mark the positions of the anticrossings 5 - 2' and 5 - 1'. (b) Current density, plotted as a function of E.

The calculated inversion peak $p_5/p_4=5.1$ lies above the experimentally measured maximum $p_5/p_4=2.58\pm0.52$ [4], and also the experimentally measured current density peak [4] is overestimated by about 40%. This is a

well known phenomenon for MC simulations of structures dominated by LO phonon-induced carrier transport [15,17], and may partly be due to the absence of broadening mechanisms in the algorithm, as discussed above. To some extent, the deviation can also be ascribed to a lower than specified free-carrier density in the sample. In addition, the experimental effective current density, which has been calculated based on an effective area, is smaller than the on-axis value in the gain medium. The simulated inversion peak[1] is shifted by -2.4 kV/cm relative to the experimental maximum, which occurs at 11.9 kV/cm, and the current density peak is shifted by a similar amount. Possible explanations are an additional parasitic resistance in the experimental structure or deviations in the growth process.
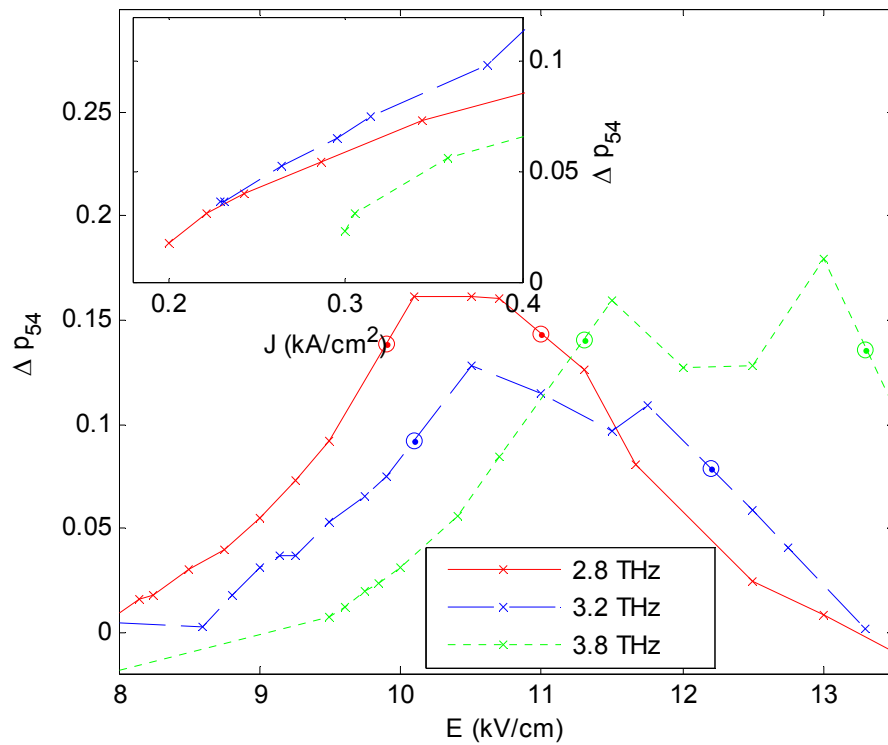

Fig. 3. Population difference between upper and lower laser level as a function of the applied field. The circles mark the positions of the anticrossings 5 - 2' and 5 - 1'. The inset shows Δp_{54} as a function of the current density close to the onset of inversion. The crosses mark the sampling points; the lines are guide to the eye.

In Fig. 3, the population difference Δp_{54} is plotted as a function of the electrical field for three THz QCLs operating at 2.8 THz [4], 3.2 THz [3] and 3.8 THz [2]. The maximum of Δp_{54} in Fig. 3(a), which occurs at an especially high bias for the 3.8 THz structure in agreement with experiment [2], is for all designs located around the two anticrossings of level 5 with the injector states. The inset shows Δp_{54} close to the onset of inversion as a function of the current density, for values ranging between the minimum value after the parasitic 1' – 4 anticrossing peak and 0.4 kA/cm^2. This corresponds to an electrical field range of 8.25-9.4, 9.15-10.4 and 9.85-10.5 kV/cm for the 2.8, 3.2 and 3.8 THz design, respectively. In the 2.8 and 3.2 THz structures, the onset of inversion

occurs at much smaller current densities than for the 3.8 THz one, which is an indication of the weaker parasitic channel 1' - 4. These findings are in agreement with the experimental results, which yield a significantly reduced threshold current for the 2.8 and 3.2 THz structures as compared to the 3.8 THz design [4].

Table 1. Overview over simulation results for the 2.8/3.2/3.8 THz structure close to the onset of inversion.

Quantity	J=0.3 kA/cm^2	J=0.4 kA/cm^2
p_5 (%)	7.5/8.2/3.5	10.6/13.8/7.9
p_4 (%)	1.6/1.5/1.2	2.1/2.5/1.3
$\eta_{inj,5}$ (%)	43.3/42.8/26.1	42.9/48.4/40.1
$\eta_{inj,4}$ (%)	14.6/15.2/22.6	16.3/18.9/13.6
$\eta_{inj,3}$ (%)	20.9/23.6/17.8	23.0/21.9/26.1
$\eta_{inj,2}$ (%)	3.5/3.2/12.2	3.4/2.2/9.3
$\eta_{inj,1}$ (%)	14.2/10.7/19.2	13.0/7.7/9.9
τ_5 (ps)	2.75/3.05/2.02	2.96/3.43/2.18
$\tau_{5\to4}$ (ps)	11.1/11.7/13.7	10.1/9.7/11.9
τ_4 (ps)	0.97/0.88/0.68	0.88/0.83/0.71
f_{54}	0.65/0.53/0.78	0.52/0.49/0.72

To further investigate the structures, we introduce the injection efficiency $\eta_{inj,i}$ from a given period into a level i of the next-lower period, defined as the ratio between the carriers injected into level i and the total amount of carriers injected into that period. An overview of the simulation results is given in Table 1. The low inversion in the 3.8 THz structure at J=0.3 kA/cm^2 can be partly attributed to the poor injection efficiency into the upper laser level $\eta_{inj,5}$, which is only 26% for the 3.8 THz design, as compared to over 40% for the other structures. This is due to the strong parasitic injection into the states below the upper laser level, as indicated by the increased $\eta_{inj,1..4}$. From Table 1 we can see that also for the 2.8 and 3.2 THz designs, the parasitic injection channels to levels 1 – 4 play a significant role in the threshold region. To obtain a high inversion, long lifetimes τ_5 and $\tau_{5\to4}$[1] are desirable, as well as a small τ_4 ensuring a fast depopulation of the lower laser level. Furthermore, the gain is directly proportional to the reduced oscillator strength f_{54} [15]. τ_5 in the 3.8 THz structure is reduced mainly due to an increased leakage to levels 3 and 1, while the values of τ_4 and f_{54} are slightly superior for this design. At low current densities, the 2.8 THz structure shows a higher value of f_{54} than the 3.2 THz laser, outweighing the somewhat lower inversion and resulting in a slightly better threshold performance, as experimentally observed [4].

---

[1] τ_5 and $\tau_{5\to4}$ are defined as the characteristic times for relaxation from level 5 to all lower levels and to level 4 alone, respectively, and already include the effect of backscattering from the final state [15].

We have also calculated the electron-lattice energy relaxation rate τ_E^{-1}.[2] Such quantity reaches its peak in the lasing region, where the phonon-assisted injection into the upper laser level and depletion of the lower laser level are the strongest. For the best of the structures (2.8 THz), a maximum τ_E^{-1} of approximately 3.8 ps^{-1} was calculated, in reasonable agreement with experiment [4]. The other two structures show a lower maximum value of τ_E^{-1} (3.3 ps^{-1}), also in qualitative agreement with the experiment.

In conclusion, we have shown that the MC simulation allows us to identify the parasitic processes affecting the operation of THz lasers, thus providing a meaningful explanation of the experimental findings.

1.4 Limiting Factors for High Temperature Operation of GaAs-based THz QCLs

As mentioned above, the low operating temperatures still remain a major problem, restricting the potential areas of application. The maximum values for THz QCLs, obtained with an optimized resonant-phonon scattering depopulation scheme, are 164 K in pulsed and 117 K in cw mode [5]. The large separation between the lower laser level and the ground states, corresponding to the LO phonon energy, ensures both efficient depletion of the lower laser level thru LO phonon scattering and reduced thermal backfilling. This overcomes the limitations associated with the conventional bound to continuum and chirped superlattice designs, where the depletion of the lower radiative state is less efficient and strong thermal backfilling of this state prevents high-temperature performance.

There has been a considerable interest in identifying the main limiting factors for high-temperature operation of the resonant-phonon depopulation scheme. The degradation in performance is mainly attributed to the decrease of the upper-state lifetime and thermal backfilling of the lower laser level, but experimental investigations could only give partial clarification [18]. In the following, we theoretically investigate the effect of increased lattice temperature on the carrier transport in such structures and specify the detrimental effects.

Here, we investigate the 3.0 THz resonant-phonon depopulation design with which the high operating temperatures mentioned above have been obtained [5]. The conduction band profile is shown in Fig. 4 at 10.8 kV/cm for a single period. The upper laser level 5 is filled from the injection states 1' and 2' (i.e., the replica of levels 1 and 2 situated in the adjacent period). Depopulation of the lower laser level 4 takes place by LO phonon scattering to levels 2 and 1 directly or via the collector state 3.

---

[2] τ_E is here calculated as $\tau_E=(E_{kin,e}-E_{kin,e}^{eq})/P_{th}$, where $E_{kin,e}$ is the total kinetic energy of the N simulated electrons and $E_{kin,e}^{eq}=Nk_BT_L$ is the equilibrium kinetic energy at lattice temperature T_L. The dissipated thermal power P_{th} is computed as the product of the calculated current and the applied voltage.
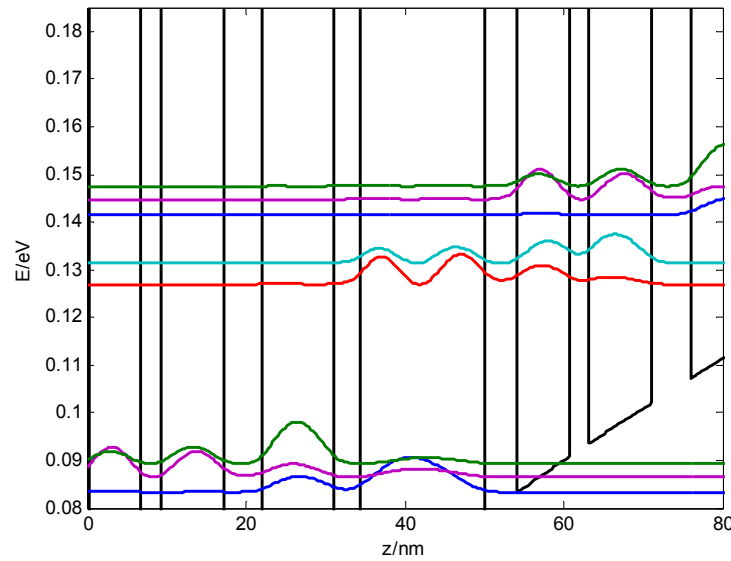
Fig. 4. Conduction band profile and probability densities of the 3.0 THz GaAs/Al$_{0.15}$Ga$_{0.85}$As phonon depopulation design at 10.8 kV/cm. The layer thicknesses in one period are 90/33/156/41/66/25/79/49 [Å]. The underlined layer is doped, the sheet density for one period is n$_{2D}$=3x10^{10} cm^{-2}.
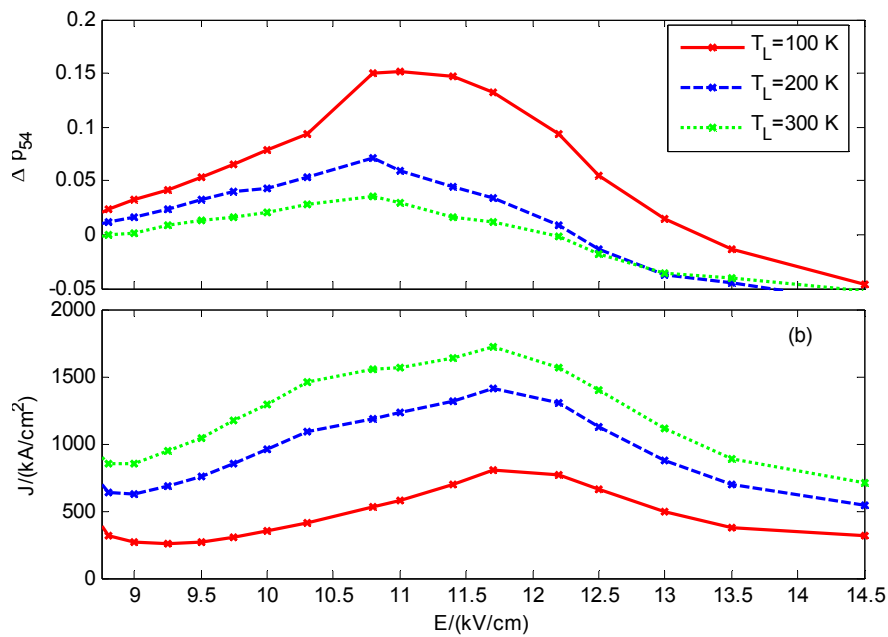

Fig. 5. Simulation results for the QCL structure as a function of the applied field for various temperatures. The crosses mark the sampling points, the lines are guide to the eye. (a) Relative population difference. (b) Current density.

In Fig. 5(a), Δp_{54} is displayed. Also shown is the current density (Fig. 5(b)). The sampling points, marked by crosses, were chosen as to avoid the excessive current spikes emerging near narrow anticrossings in MC simulations, as discussed above. The increase in current density for rising lattice temperature can mainly be attributed to enhanced LO phonon

scattering, while the inversion decreases due to a growing thermalization between the levels.
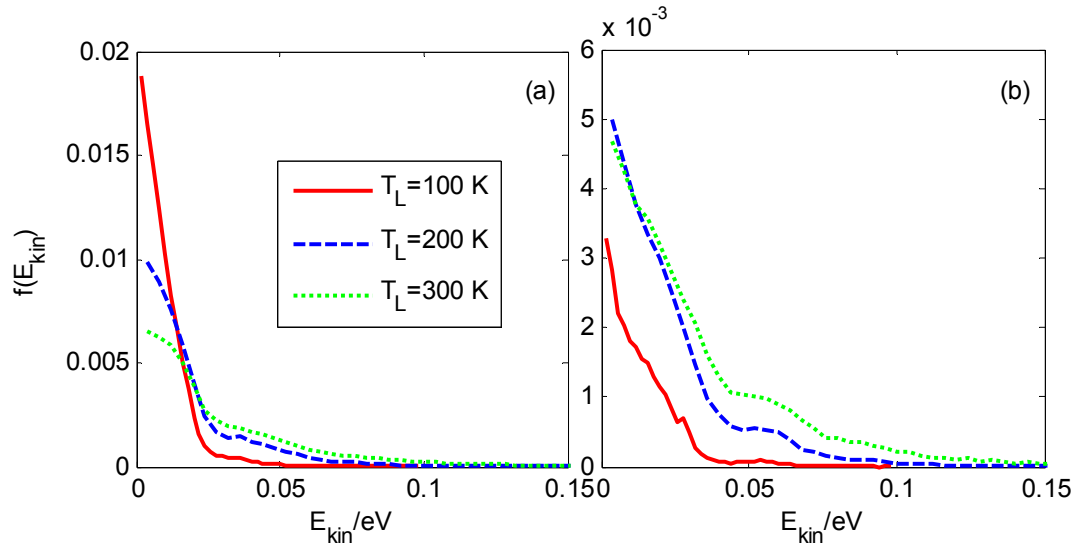

Fig. 6. Electron distribution functions of the (a) upper and (b) lower laser level as a function of the kinetic energy for an applied field of 10.8 kV/cm and various lattice temperatures.

An evaluation of the numerical scattering rates shows that while intrasubband scattering is governed by electron-electron (e-e) interaction, intersubband transport is mainly mediated thru LO phonons for the doping level and temperatures considered, even in the case of closely aligned states. Fig. 6 displays the electron distribution functions for the upper and lower laser levels at a bias of 10.8 kV/cm, where Δp_{54} in Fig. 5 reaches its peak. The filling of the laser levels occurs predominantly from level 1' into 5 and from levels 5,2' into 4 thru both LO phonon emission and absorption. The hot phonon effect in such structures gives rise to an increased LO phonon occupation [19]. This mechanism leads to an increased carrier injection at kinetic energies around 30 meV (level 5) and 50 meV (level 4) due to the stronger LO phonon absorption, yielding bumps in the distribution functions. Since the electrons are not quite in thermal equilibrium within the subbands, the distributions can only to some extent be characterized by temperatures. A least square fit of the distributions in level 5 (4) yields electron temperatures of 122 (169), 206 (273) and 322 (376) K for lattice temperatures of 100, 200 and 300 K, but a fit exclusively to the low-energy electrons or the high-energy tail can yield significantly different results [20]. Typically, the determined electron temperatures are in between the lattice temperature and roughly 100 K above, depending on the subband and the applied bias.

Table 2. Overview over the simulation results for the 3.0 THz structure at 10.8 kV/cm.

Quantity	T_L=100 K	T_L=200 K	T_L=300 K
p_5 (%)	19.7	18.7	18.6
p_4 (%)	4.6	11.6	15.0
$\eta_{inj,5}$ (%)	55.9	56.6	57.4
$\eta_{inj,4}$ (%)	20.9	23.5	24.0
J (kA/cm^2)	0.53	1.19	1.55

In Tables 2 and 3, an overview over the simulation results for the 3.0 THz structure is given. The relative population of the upper laser level p_5 is proportional to $\eta_{inj,5}J/r_5$. Here, $\eta_{inj,5}$ is the relative injection efficiency from the previous period into level 5, and $r_5 = r_{5\rightarrow4} + r_{5\rightarrow3} + \ldots$ is the inverse of the characteristic lifetime, i.e., the effective relaxation rate from level 5 to the lower levels in this period. While $\eta_{inj,5}$ changes only slightly from 55.9% to 57.4% for temperatures between 100 and 300 K, the current density J increases from 0.53 to 1.55 kA/cm^2. This can mainly be attributed to enhanced LO phonon scattering. Since r_5 increases by the same relative amount (see Table 3), p_5 remains almost constant (19.7%...18.6%). From Table 3, we see that the main depletion channels of the upper laser level are the parasitic transitions to levels 4 and 3. The increased lattice temperature leads to broader kinetic electron distributions, thus more electrons have sufficient kinetic energy to participate in LO phonon emission events. On the other hand, p_4 increases from 4.6% to 15.0%, since the corresponding relaxation rate r_4 does not increase sufficiently to compensate the increased current. This is due to the backscattering from the lower levels characterized by $r_{4\leftarrow}$ (with $r_4 = r_{4\rightarrow} + r_{4\leftarrow}$), which strongly increases with temperature. Thus higher lattice temperatures lead to a decreased population difference $p_5 - p_4$ and a smaller gain.

Table 3. Electron intersubband scattering rates at different lattice temperatures T_L for the 3.0 THz structure; the bias is 10.8 kV/cm.

T_L	r_5 (ps^{-1})	$r_{5\rightarrow4}$ (ps^{-1})	$r_{5\rightarrow3}$ (ps^{-1})	r_4 (ps^{-1})	$r_{4\rightarrow}$ (ps^{-1})	$r_{4\leftarrow}$ (ps^{-1})
100 K	0.31	0.13	0.12	1.06	1.29	-0.23
200 K	0.75	0.37	0.31	1.09	1.93	-0.84
300 K	1.00	0.51	0.42	1.14	2.76	-1.62

To reduce the effect of backscattering to the lower laser level, a double-resonant-phonon depopulation structure has been realized, where the depletion from the lower laser level to the ground states occurs via an intermediate state, involving two LO phonon emission events (device B in [18]). We can modify our structure to a double-resonant-phonon design by simply increasing the energy gap between levels 4 and 3 to the LO phonon energy of 36 meV, keeping the other energy distances and all the wave functions unchanged (Fig. 7). While there may not exist a corresponding QCL structure featuring exactly this energy level scheme, the chosen approach ensures that all the observed changes are exclusively due to the increased energy gap, thus facilitating the interpretation of the results. In Table 4, an overview over the simulation results for the modified structure is given. A comparison with Table 2 shows that the injection efficiency $\eta_{inj,5}$ remains similar to that of the original structure, but the current density is significantly higher. This results from the enhanced average kinetic electron energy due to the larger potential drop over the period, leading to an overall increase in LO phonon scattering. A comparison between Tables 3 and 5 shows that the LO phonon resonance between levels 4 and 3 leads to an enhanced rate r_4 and thus as hoped to a more efficient depletion of the lower laser level, but also to

an increased parasitic leakage from the upper laser level, especially due to the increased LO phonon scattering rate $r_{5\to3}$. This results in both a decreased p_5 (9.7%...15.7%) and p_4 (2.3%...10.1%) in the modified structure. Only for high temperatures around 300 K, the population difference p_5-p_4, and thus the gain, is larger than for the original structure.
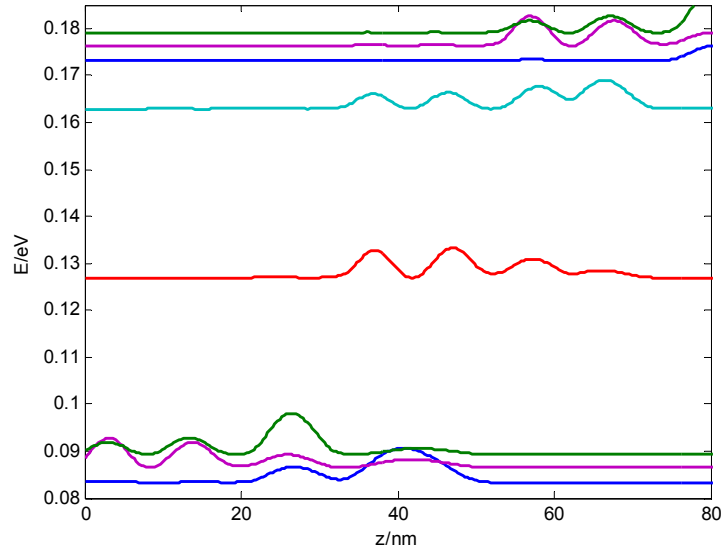

Fig. 7. Conduction band profile and probability densities of the double-resonant-phonon depopulation design at 10.8 kV/cm.

Table 4. Overview over the simulation results for the double-resonant-phonon depopulation structure at 10.8 kV/cm.

Quantity	T_L=100 K	T_L=200 K	T_L=300 K
p_5 (%)	9.7	13.7	15.7
p_4 (%)	2.3	6.6	10.1
$\eta_{inj,5}$ (%)	50.9	55.6	56.9
$\eta_{inj,4}$ (%)	14.9	19.4	21.3
J (kA/cm^2)	1.22	1.81	2.14

Table 5. Electron intersubband scattering rates at different lattice temperatures T_L for the double-resonant-phonon depopulation structure; the bias is 10.8 kV/cm.

T_L	r_5 (ps^{-1})	$r_{5\to4}$ (ps^{-1})	$r_{5\to3}$ (ps^{-1})	r_4 ps^{-1})	$r_{4\to}$ (ps^{-1})	$r_{4\leftarrow}$ (ps^{-1})
100 K	1.33	0.33	0.95	3.02	5.01	-1.99
200 K	1.53	0.58	0.89	2.30	5.26	-2.96
300 K	1.62	0.71	0.85	2.04	5.86	-3.82

In summary, the effects restricting high-temperature operation in GaAs-based THz QCLs have been quantified. We have shown that the main detrimental mechanisms are the increased leakage of the upper laser level and the backfilling of the lower laser level. The simulations indicate that for achieving higher operation temperatures with this type of structure, the only possibility is a further reduction of optical losses.

12

2. Investigation of Si/SiGe THz quantum cascade structures

Unlike the GaAs-based QCLs discussed above, Si/SiGe quantum cascade structures are based on hole transport in the valence bands. A significant difference is the absence of polar phonon scattering in these structures, which might lead to a weaker temperature dependence of the operational behavior. However, as mentioned above, no lasing, but only electroluminescence could be achieved in Si/SiGe structures. [7,8].

We have performed Monte Carlo simulations of the hole transport in such structures. Our approach is based on envelope functions, since a full k.p calculation, including all the important effects like carrier-phonon and carrier-carrier scattering, seems too demanding regarding the developmental and numerical complexity.

2.1 The Monte Carlo program

Here, a Schrödinger-Poisson solver is used to determine the heavy hole (HH) and light hole (LH) wave functions within the effective mass approximation, which are needed to calculate the form factors for hole-phonon and hole-hole interactions. We have taken care that the energy levels and wave functions obtained with the simplified model do not differ significantly from those of the more precise k.p approach. In particular, the adequate effective masses and band offsets for the HH and the LH bands have been extracted from the k.p approach. Unlike for GaAs-based QCLs, transitions within the HH and LH bands, and between them, are mediated by non polar optical phonons. Both inter- and intraband optical phonon scattering is taken into account. Three optical phonon branches have been implemented, corresponding to Ge-Ge, Si-Si, and Ge-Si interatomic vibrations. Furthermore, acoustic phonon and carrier-carrier scattering is accounted for.

2.2 Results

We have simulated a 7.0 THz Si/SiGe resonant-phonon-depopulation structure. Fig. 8 shows the relevant hole states in a period of the structure for an applied field of 48 kV/cm. The probability densities of the heavy hole (HH) and light hole (LH) states, as well as the valence band edges for heavy and light holes, are denoted by solid and dashed lines, respectively. As pointed out above, the calculation is based on an effective mass envelope function approach. The laser transition in this structure takes place between levels 5 and 4. The depopulation of the lower laser level 4 to the ground states 1 and 2 via the collector state 3 is mainly mediated by optical phonon scattering.

```
Report                    Modeling of THz quantum cascade lasers
Grant 063008                   for room temperature operation
```
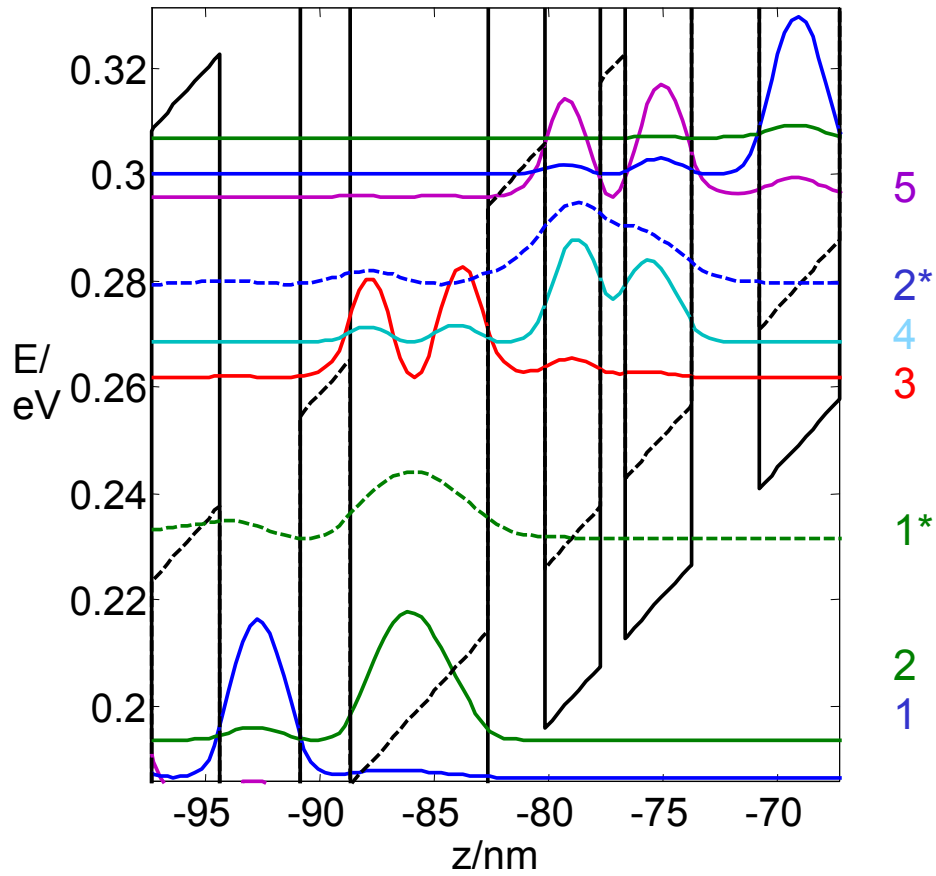
Fig. 8. Valence band profile and probability densities of a 7.0 THz QCL based on a phonon depopulation scheme at 48 kV/cm. Shown are the heavy hole (solid lines) and the light hole (dashed lines) subbands.

Figure 9 shows MC simulation results for the 7.0 THz structure at lattice temperatures of 100 and 300 K. In Fig. 9(a), the difference of the relative population in the upper (p_5) and lower (p_4) laser levels is displayed as a function of the applied field, with $\Delta p_{54}=p_5-p_4$. The current density is shown in Fig. 9(b). For both temperatures, the maximum population difference is obtained at a bias of 43 kV/cm.

An evaluation of the numerical scattering rates shows that intersubband transport is mainly mediated thru acoustic and optical phonons. Only for transitions between closely aligned states, like the carrier injection from states 1' and 2' into the upper laser level, also carrier-carrier scattering plays a significant role. Fig. 10 displays the hole distribution functions for the upper and lower laser levels at a bias of 43 kV/cm, where Δp_{54} in Fig. 9 reaches its peak. As discussed in Section 1.4, the carriers are not quite in thermal equilibrium within the subbands, and thus the distributions can only to some extent be characterized by temperatures. A least square fit of the distributions in level 5 (4) yields carrier temperatures of 172 (228) and 284 (367) K for lattice temperatures of 100 and 300 K.

```
Report                    Modeling of THz quantum cascade lasers
Grant 063008                    for room temperature operation
```
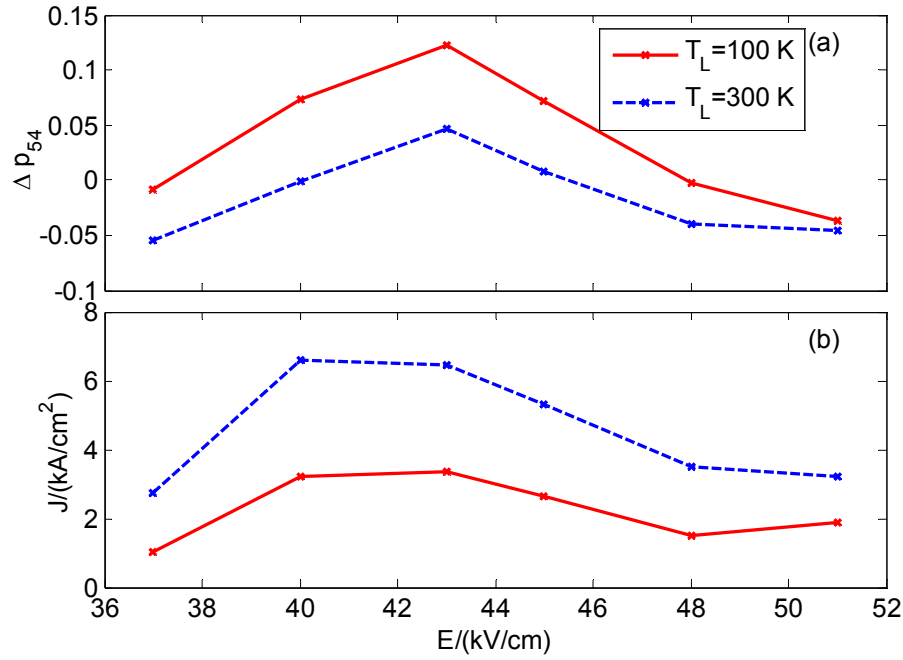
Fig. 9. Simulation results for the Si/SiGe structure as a function of the applied field (E) for lattice temperatures of 100 and 300 K. The crosses mark the sampling points; the lines are guide to the eye. (a) Relative population difference between the upper and lower laser level. (b) Current density, plotted as a function of E.
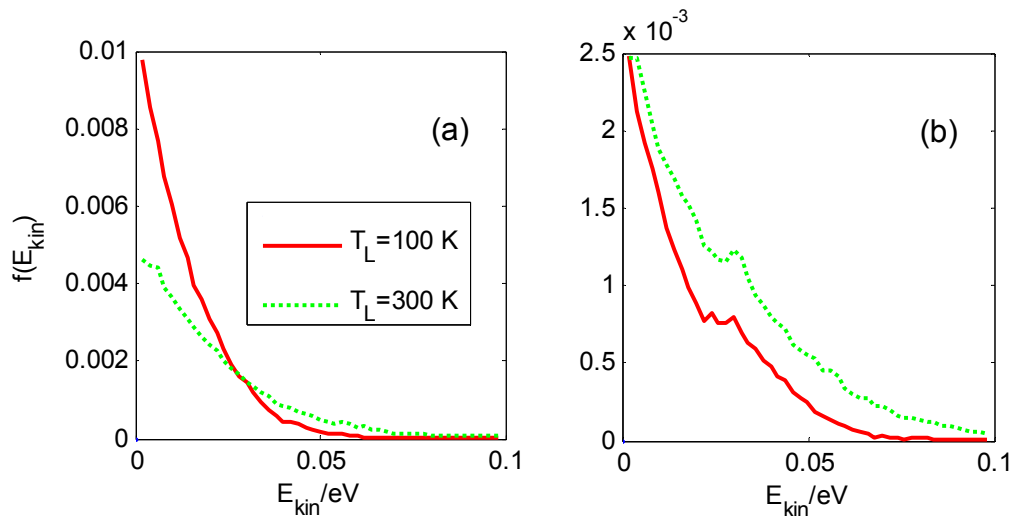

Fig. 10. Hole distribution functions of the (a) upper and (b) lower laser level as a function of the kinetic energy for an applied field of 43 kV/cm and lattice temperatures of 100 and 300 K.

In Tables 6 and 7, an overview over the simulation results for the Si/SiGe quantum cascade structure is given. Here, $\eta_{inj,5}$ is again the relative injection efficiency from the previous period into level 5, and $r_5 = r_{5 \to 4} + r_{5 \to 3} + \ldots$ is the effective relaxation rate from level 5 to the lower levels in this period. Similarly as for the GaAs QCL (see Tables 2 and 3), $\eta_{inj,5}$ changes only slightly from 51.3% to 47.0% for temperatures between 100 and 300 K, while the current density J almost doubles from 3.37 to 6.45 kA/cm^2. Here, this is due to enhanced optical and acoustic phonon scattering. Since the depletion of the

upper laser level, characterized by r_5, strongly increases (see Table 7), p_5 somewhat decreases from 18.2% to 14.0%, with the main depletion channels given by the parasitic transitions to levels 4 and 3. The occupation of the lower laser level p_4 increases from 6.0% to 9.3%, since the corresponding relaxation rate r_4 rises much more weakly with temperature than the total current, which is due to the increased backscattering from the lower levels characterized by $r_{4\leftarrow}$ (with $r_4=r_{4\rightarrow}+r_{4\leftarrow}$). In summary, increased lattice temperatures result in a decreased population difference p_5-p_4, and thus a smaller gain.

Table 6. Overview over the simulation results for the Si/SiGe structure at 43 kV/cm.

Quantity	T_L=100 K	T_L=300 K
p_5 (%)	18.2	14.0
p_4 (%)	6.0	9.3
$\eta_{inj,5}$ (%)	51.3	47.0
$\eta_{inj,4}$ (%)	18.0	18.4
J (kA/cm^2)	3.37	6.45

Table 7. Intersubband scattering rates at different lattice temperatures T_L for the Si/SiGe structure; the bias is 43 kV/cm.

T_L	r_5 (ps^{-1})	$r_{5\rightarrow4}$ (ps^{-1})	$r_{5\rightarrow3}$ (ps^{-1})	r_4 (ps^{-1})	$r_{4\rightarrow}$ (ps^{-1})	$r_{4\leftarrow}$ (ps^{-1})
100 K	0.59	0.26	0.20	1.40	1.87	0.47
300 K	1.36	0.59	0.45	1.67	3.00	1.33

In conclusion, our simulation based on an effective mass approach suggests that although LO phonon scattering is absent in Si/SiGe structures, the carrier transport is still dominated by (acoustic and optical) phonon scattering in the investigated design. Thus the main detrimental mechanisms at high operating temperatures are, as for the GaAs-based structure, the increased leakage of the upper laser level and the backfilling of the lower laser level.

16

Report
Grant 063008
Modeling of THz quantum cascade lasers
for room temperature operation

REFERENCES

[1] R. Köhler, A. Tredicucci, F. Beltram, H. E. Beere, E. H. Linfield, A. Giles Davies, D. A. Ritchie, R. C. Iotti, and F. Rossi, *Terahertz semiconductor-heterostructure laser*, Nature 417, 156-159 (2002).

[2] B. S. Williams, S. Kumar, H. Callebaut, Q. Hu, and J. L. Reno, Appl. Phys. Lett. **83**, 5142 (2003).

[3] S. Kumar, B. S. Williams, S. Kohen, Q. Hu, and J. L. Reno, Appl. Phys. Lett. **84**, 2494 (2004).

[4] M. S. Vitiello, G. Scamarcio, V. Spagnolo, B. S. Williams, S. Kumar, Q. Hu, and J. L. Reno, Appl. Phys. Lett. **86**, 111115 (2005).

[5] B. S. Williams, S. Kumar, Q. Hu, and J. L. Reno, Opt. Expr. **13**, 3331 (2005).

[6] G. Dehlinger, L. Diehl, U. Gennser, H. Sigg, J. Faist, K. Ensslin, D. Grützmacher and E. Müller, *Intersubband electroluminescence from silicon-based cascade structures*, Science **270**, 2277-2280 (2000).

[7] S. A. Lynch, R. Bates, D. J. Paul, D. J. Norris, A. G. Cullis, Z. Ikonic, R. W. Kelsall, P. Harrison, D. D. Arnone, and C. R. Pidgeon, *Intersubband electroluminescence from Si/SiGe cascade emitters at terahertz frequencies*, Appl. Phys. Lett. **81**, 1543-1545 (2002).

[8] R. Bates, S. A. Lynch, D. J. Paul, Z. Ikonic, R. W. Kelsall, P. Harrison, S. L. Liew, D. J. Norris, A. G. Cullis, W. R. Tribe, and D. D. Arnone, *Interwell intersubband electroluminescence from Si/SiGe quantum cascade emitters*, Appl. Phys. Lett. **83**, 4092-4094 (2003).

[9] F. Compagnone, A. Di Carlo, and P. Lugli, Appl. Phys. Lett. **80**, 920 (2002).

[10] M. Manenti, F. Compagnone, A. Di Carlo, P. Lugli, G. Scamarcio, and F. Rizzi, Appl. Phys. Lett. **82**, 4029 (2003).

[11] R. Köhler, R. C. Iotti, A. Tredicucci, and F. Rossi, Appl. Phys. Lett. **79**, 3920 (2001).

[12] S. M. Goodnick and P. Lugli, Phys. Rev. B **37**, 2578 (1988).

[13] M. Moško, A. Mošková, and V. Cambel, Phys. Rev. B **51**, 16860 (1995).

[14] S. M. Goodnick and P. Lugli, Appl. Phys. Lett. **51**, 584 (1987).

[15] H. Callebaut, S. Kumar, B. S. Williams, Q. Hu, and J. L. Reno, Appl. Phys. Lett. **83**, 207 (2003).

[16] T. Kubis and P. Vogl, Journal of Computational Electronics, in press.

[17] R. Köhler, A. Tredicucci, F. Beltram, H. E. Beere, E. H. Linfield, A. G. Davies, D. A. Ritchie, R. C. Iotti, and F. Rossi, Nature **417**, 156 (2002).

[18] B. S. Williams, S. Kumar, Q. Qin, Q. Hu, and J. L. Reno, "Terahertz quantum cascade lasers with double-resonant-phonon depopulation," Appl. Phys. Lett. **88**, 261101 (2006).

[19] J. T. Lü and J. C. Cao, Appl. Phys. Lett. **88**, 061119 (2006).

[20] C. Jirauschek, G. Scarpa, P. Lugli, and M. Manenti, to appear in Journal of Computational Electronics.